

Raman spectroscopic characterization of necrotic cell death

Nagapratima Kunapareddy

James P. Freyer

Judith R. Mourant

Los Alamos National Laboratory
Bioscience Division, MS E535
Los Alamos, New Mexico 87545

Abstract. Raman spectroscopy has been used to estimate the biochemical changes due to necrosis in an *in vitro* model system comprised of a human malignant melanoma cell line (MEL-28). Combined oxygen and glucose deprivation was used to simulate necrotic cell death in tumors. Raman spectroscopy measurements of nonproliferating live cells and dead cells were made at 24, 48, and 72 hours. Quantitative estimates of the biochemical composition of live and dead cells were made by fitting cell spectra to the basis spectra of protein, lipid, RNA, DNA, and glycogen. A decrease in the relative amount of lipid and RNA, and an increase in the relative protein content, were observed in dead cells. A comparison of the spectra indicated the existence of conformational changes in protein and nucleic acids in dead cells. These results suggest that Raman spectroscopy could be used to detect necrotic cell death in tumors. © 2008 Society of Photo-Optical Instrumentation Engineers. [DOI: 10.1117/1.2978061]

Keywords: cell death; oxygen and glucose deprivation; necrosis; Raman spectroscopy; biochemical analysis; biological cells.

Paper 08016R received Jan. 13, 2008; revised manuscript received Apr. 4, 2008; accepted for publication Apr. 7, 2008; published online Sep. 17, 2008.

1 Introduction

The balance between cell proliferation and cell death determines tumor growth. Most modalities of cancer therapy, especially chemotherapy and radiotherapy, aim at disrupting this balance by interfering with the proliferation mechanism or by compromising the structural integrity of the cells. Ideally, treatment sets into motion the cellular and molecular series of events that result in cell death. The death of tumor cells with minimal damage to healthy cells is the goal of chemotherapy and radiotherapy.

Necrosis is one of the modalities of cell death following treatment, and hence, identifying necrosis is clinically valuable. From a treatment and diagnostic perspective, an estimate of tumor necrosis is an indicator of treatment efficacy and tumor response.¹⁻³ In the case of neo-adjuvant therapy in sarcomas, determination of treatment-induced necrosis volume has become the most reliable method by which an objective assessment of chemo- and radio-sensitivity is made.⁴⁻⁶ Currently, estimates of tissue necrosis are routinely made via histopathological examination of biopsies. There are several magnetic resonance imaging (MRI) methods capable of detecting necrosis in tumors,⁷⁻⁹ but the identification of necrosis via MRI is challenging because it can closely resemble recurrent tumors^{10,11} and requires routine access to expensive MRI instruments. A noninvasive method of detecting cell death, such as Raman spectroscopy, would reduce patient trauma during biopsies, reduce the subjectivity inherent to biopsy-based diagnosis, and enable real-time treatment monitoring and diagnosis.

In this study, combined oxygen and glucose deprivation (OGD) was used to induce cell death. Cell death by OGD has been previously used as a model for necrosis.¹² Mammalian cells generate energy in the form of adenosine triphosphate (ATP) by two mechanisms— aerobic respiration and glycolysis. Cells can generate energy in the absence of either oxygen or glucose, but not both. Simultaneous oxygen and glucose deprivation leads to a severe energy deficit, and in the absence of energy, cellular processes come to a halt and the cells die. Human melanoma cells (MEL-28) were chosen for this study, because most cancers originate in the epithelial layers of tissue.

In this study, we have demonstrated the use of Raman spectroscopy to identify and quantify the spectroscopic changes that occur due to cell death by combined oxygen and glucose deprivation. Quantitative estimates of the biochemical changes were obtained using methods demonstrated previously.¹³⁻¹⁵

2 Materials and Methods

2.1 Monolayer Cell Culture and Cell Preparation

MEL-28, an adherent, human melanoma cell-line of dermal origin, was used for this study. Cells were obtained from the American Tissue Culture Collection (catalog no. HTB-72). The cells were cultured in α -MEM supplemented with 10% fortified bovine calf serum (Hyclone) and antibiotics (5 μ g/ml streptomycin and 50 IU/ml penicillin). The cells were cultured as monolayers on polystyrene culture flasks in a 37 °C humidified incubator with 5% CO₂ and air. Exponentially growing MEL-28 cell cultures have a doubling time of

Address all correspondence to: Judith R. Mourant, Los Alamos National Laboratory, Bioscience Division, MS E535, Los Alamos, New Mexico 87545. E-mail: jmourant@lanl.gov

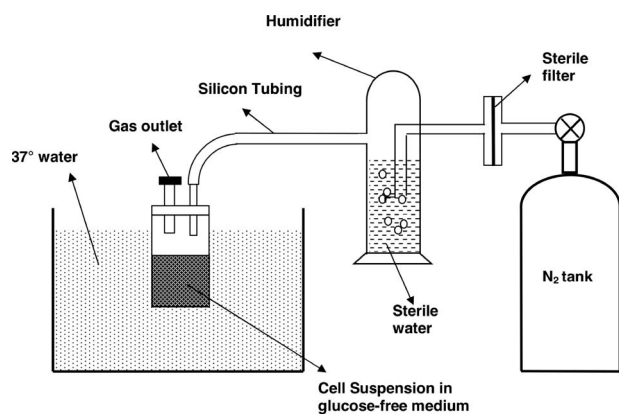


Fig. 1 Setup for the oxygen-glucose deprivation experiments.

approximately 10 hours. Cultures were split on a biweekly basis to maintain them in the exponential stage of growth. Cultures in the plateau phase of growth were used for these experiments because it is the nonproliferating cells in tumors that eventually die by necrosis. Growth curve experiments showed that MEL-28 cells reached the plateau stage at a cell density of 1.9×10^5 cells/cm². Based on these data, plateau cells were harvested 1 to 2 days after they became confluent.

Cell suspensions were obtained by treating the monolayer cultures for 7 minutes with 0.25% trypsin in a phosphate buffer (pH 7.4) containing 1 mM EDTA and 25 mM HEPES, followed by the addition of cold medium. Cell suspensions were passed twice through an 18-gauge needle, which can separate aggregates but does not damage the cells.¹⁶ The cell suspensions were then centrifuged at $1200 \times g$ for 10 min into a pellet. The cell pellet was resuspended in phosphate buffered saline (PBS) and centrifuged again to remove residual medium. For Raman measurement of live cells, a cell pellet of 2×10^8 cells was prepared. The cell pellet was suspended in PBS and spun down into a sample cell. For setting up the OGD experiments, the pellet of plateau cells was resuspended in alpha-MEM without glucose to a volume of 3.5 ml with a concentration of 1.5 to 2×10^8 cells/ml.

To count the cells, a 0.5-ml sample of the cell suspension added to 20 ml of PBS was counted using an electronic particle counter equipped with a pulse-height analyzer (model Z2, Beckman Coulter). Three counts were made for each sample and averaged. A cell volume distribution was obtained, and size thresholds were set to exclude acellular debris. The particle counter was calibrated by measuring several sizes of polystyrene microspheres. Absolute mean cell volumes and cell concentrations were determined.

2.2 Oxygen and Glucose Deprivation

A custom-built chamber was used to expose viable cells to an oxygen- and glucose-free environment, as shown in Fig. 1. The cell suspension, in a glucose-free medium, was loaded into a glass vial, and the vial was sealed with a rubber cap. Nitrogen gas (95% N₂, 5% CO₂) was supplied to the vial using a 22-gauge needle to keep the cells in an oxygen-free environment. The tip of the syringe needle was positioned well above the cell suspension to prevent clogging. To prevent the cells from drying out, the nitrogen tank was connected to

a humidifier filled with sterile water via a sterile 0.22 μ m pore filter and a short length of gas-impermeable tubing (PharMed BPT, Cole-Parmer). Prior to starting the experiment, sterile nitrogen gas was bubbled through the humidifier for two hours to displace all the dissolved oxygen. A 22-gauge syringe needle capped with a small amount of cotton was inserted through the rubber seal to allow gas flow out of the chamber. This entire arrangement was placed in a 37 °C water bath. The vial was inspected at regular intervals to ensure that no cell drying occurred. Samples of cells for counting and viability assay were drawn from the vial at 24, 48, and 72 hours using a sterile 18-gauge needle. For Raman measurements, 0.5 ml of the cell suspension was removed and transferred to a sample cell. Measurements of live cells in the plateau phase of growth were made as a control.

2.3 Determination of Cell Death Rate

To assess cell viability, 10- μ l samples of cells were drawn from the oxygen and glucose deprivation chamber at regular intervals. Viability was assessed using the trypan blue exclusion assay and examination of the stained cell suspension on a hemacytometer slide. approximately 200 to 400 cells were counted per sample, and the fraction of dye-infiltrated, and therefore dead, cells was determined.

2.4 Flow Cytometry

Cell cycle distributions were obtained by using standard flow cytometric analysis. Briefly, 10^6 cells were fixed in 70% ethanol and refrigerated. Fixed samples were prepared for analysis by centrifuging the cells to a pellet for 10 min at $1200 \times g$ and resuspending them in 1 ml of staining solution containing 50 μ g/ml of propidium iodide (PI) and 100 μ g/ml of RNase in PBS containing Ca²⁺ and Mg²⁺. The stained samples were stored overnight at 5 °C and analyzed on a flow cytometer (FACS Calibur, Becton Dickinson) using a 488-nm air-cooled argon-ion laser and a 585-nm emission filter. DNA histograms with more than 10^4 cells were obtained and were very similar to those on the left side of Fig. 1 in Short 2005.¹⁴ DNA histograms were fit to obtain cell-cycle distributions using automated routines in WinList (Verity Software House) and ModFit-LT (Verity Software House) after gating out debris and aggregates.

2.5 Raman Instrumentation

The bench-top Raman system used a 785-nm continuous-wave diode laser (Invictus, Kaiser Optical Systems) as the excitation source. The laser was coupled via a multimode fiber to a probe head. The probe head was equipped with a holographic grating to eliminate the intrinsic Raman signal of the fiber. The excitation light was focused on the sample using an $f/0.7$ aspheric condenser lens with a focal length of 10.8 mm (Edmund Industrial Optics). Backscattered light was collected through the same lens. The excitation light was eliminated via a pair of notch filters. The probe head was connected via a fiber optic to an imaging spectrometer (HoloSpec, $f/1.8$, Kaiser Optical Systems). The spectrometer was equipped with a 100- μ m internal slit, another notch filter for eliminating 785-nm light, and a transmissive holographic grating covering the wavenumber region 790 to 1065 nm (100 to 3350 cm⁻¹). The spectral resolution, defined as twice

the spectral bandpass (full-width at half-maximum), was approximately 5 cm^{-1} . The spectrometer was coupled to a 1340×100 pixel deep-depletion, back-illuminated, liquid-nitrogen cooled, charge-coupled detector (CCD) connected to a ST-133 controller (Spec-10, Princeton Instruments). The sample cell was a 1-cm-diameter by 1-cm-deep open-face cylindrical receptacle made of black delrin. The volume of the sample probed was approximately 0.008 mm^3 , based on estimates of the beam diameter and the penetration depth. Plateau cells had an average volume of $1840\text{ }\mu\text{m}^3$ (calculated from an average of three measurements). Assuming an interstitial volume equal to the cellular volume, the sampled volume was estimated to contain ~ 2200 cells.

2.6 Data Collection Protocol

All spectra were collected with laser powers of 190 to 200 mW. This laser power does not cause a significant increase in the sample temperature due to the extremely low absorption of the sample at 785 nm. Water is the primary constituent of the sample that absorbs at this wavelength. The sample cell was kept in an ice water bath at all times. The probe head was held vertically above the sample cell such that the sample cell was illuminated from the top and backscattered light was collected. The distance of the sample cell from the probe head was adjusted to maximize signal intensity.¹³ The narrow noise spikes that arose from “cosmic rays” were corrected using a temporal filter. A calibrated halogen tungsten lamp (Optronics Laboratories, Inc.) that was traceable by the National Institute of Standards and Technology (NIST) was measured to determine and correct for system response. Lamp spectra were collected for a total measurement time of 5 min. A spectrum of a solution of $0.12\text{-}\mu\text{m}$ -diameter polystyrene beads in PBS was measured for wavelength calibration. Spectra of the empty sample cell, the buffer (PBS) in the sample cell, and the background (i.e., laser off) were each collected with a 1-min total measurement time. The empty sample cell signal was composed of Raman scattering and fluorescence from the system optics with no contribution from the sample cell. Two spectra of each sample of live or dead cells were collected with 10-min integration times at different points in the sample. Spectra were also taken to correct for small variations over time in the efficiencies of individual CCD pixels. Light from a flashlight was bounced off a piece of Spectralon (Labsphere) and measured for 30 s immediately before or after measuring the buffer and the empty cell, and before and after measuring the sample.

2.7 Data Analysis

The methods for converting spectral data to biochemical components have been previously described.^{13,15} Spectral regions were chosen for data fitting based on the occurrence of Raman bands; regions where there were no bands of interest were excluded for the purpose of data fitting. The spectral regions used in the fits were 450 to 1785 cm^{-1} (low wavenumber region) and 2550 to 3130 cm^{-1} (high wavenumber region). Corrected Raman spectra were fit to a linear combination of biochemical components (protein, lipid, DNA, RNA, and glycogen), empty sample cell, buffer, and intrinsic fluorescence. The concentration of the biochemical components was constrained to be greater than or equal to zero during fits. Nine-

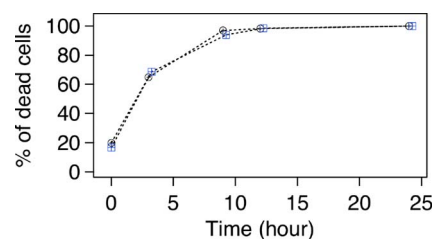


Fig. 2 Dead-cell fraction assessed by the trypan blue dye exclusion assay. Two distinct time course results are shown. The dead-cell fractions for one of the experiments was collected 15 min later than the first set with the exception of the initial time point.

teen parameters were used in the fitting routine—five for the biochemical components, one for the buffer, one for the spectrum of the system optics (i.e., the empty sample cell), and six each for modeling the polynomial for fluorescence in both wavenumber regions. Several different initial conditions were used to ensure that the algorithm found a global minimum. The data fits used the Levenberg-Marquardt algorithm as implemented in Igor Pro (Wavemetrics, Inc).¹⁷ Relative amounts of biochemical components were calculated from the fit coefficients. We have previously shown that biochemical composition determined by spectra deconvolution accurately reflects the composition estimated by sample extraction and independent analysis.¹⁵

For examination of the spectra without data fitting, the Raman spectra of live and dead cells were normalized to the peak value at 2933 cm^{-1} and smoothed using a three-point boxcar sliding average. Normalization was performed to implement a relatively simple technique, because normalized measurements are much easier to make than unnormalized measurements (although we have performed unnormalized measurements in the past.¹⁵). The position of the strongest signal in the high wavenumber region is 2933 cm^{-1} ; therefore, using this peak for normalization introduces the least amount of noise into the data.

3 Results

3.1 Time Course of Cell Death

Time course experiments were performed to estimate the rate of cell death. As shown in Fig. 2, it was found that within 12 hours, 98% of the cells died, and within 24 hours, essentially all the cells were dead.

In examining the time course of cell death, the time for all oxygen and glucose to be depleted from the medium should be considered. Although the medium used to incubate the cells was free of glucose, a small amount of glucose was present due to the addition of serum. The medium also initially contained dissolved oxygen. It is assumed that the oxygen in the air space of the vial was not available for cellular metabolism. Values of glucose and dissolved oxygen concentrations in a glucose-free medium obtained from previous work¹⁸ were 5.5×10^{-7} Mole/ml and 2.2×10^{-7} Mole/ml, respectively. Using these values, it was found that the times required for the cells to consume all of the oxygen and glucose in the media were 1 to 1.4 and 9 to 12 seconds, respectively, for an initial cell concentration of 1.5 to 2×10^8 . These estimates may be off slightly because the rates of oxygen and

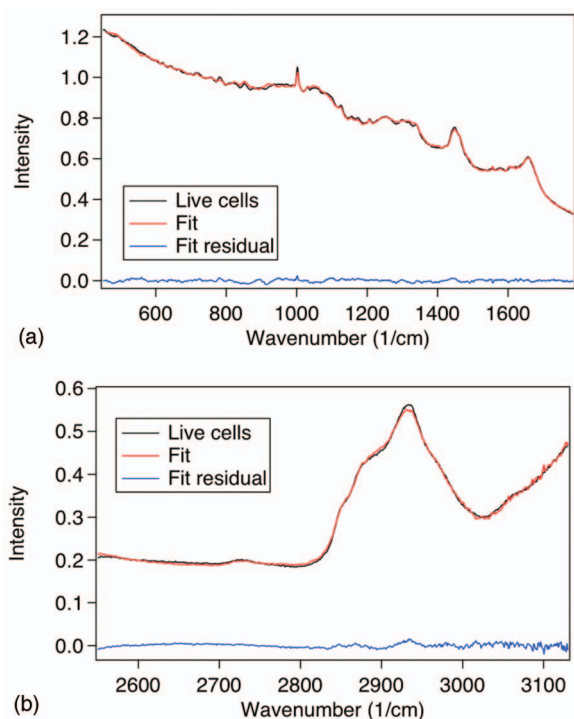


Fig. 3 Example of Raman data of live cells and the corresponding fit and fit residual: (a) 450 to 1785 cm^{-1} , and (b) 2550 to 3130 cm^{-1} .

glucose consumption do not depend only on their individual concentrations; the rate of consumption of one may also vary inversely with the concentration of the other.¹⁸ Also, the oxygen concentration would have reached zero even faster, since the medium was not air-equilibrated (as the calculation above assumes) but had been exposed to a gas phase with no oxygen for two hours prior to the addition of cells. In any case, these estimates clearly indicate that cellular metabolism had reduced the concentrations of both oxygen and glucose in the medium to zero in less than a minute.

3.2 Cell Cycle Analysis

The cells used in the OGD experiments were in the plateau growth phase, and control Raman spectral measurements were made of plateau-phase cells. To verify that the cells were not proliferating, DNA content measurements of plateau cells were made. Plateau cells had $89.63 \pm 4.46\%$ cells in the G_0 phase, $7.65 \pm 3.30\%$ cells in the G_2 phase of the cell cycle, and $2.51 \pm 2.19\%$ cells in the S phase. Means and standard deviations were calculated from four separate experiments.

3.3 Estimates of the Relative Amounts of Biochemical Components in Live and Dead Cells

Raman measurements of dead cells were made at 24, 48, and 72 hours after oxygen and glucose deprivation, as well as of live plateau cells. Individual spectra were fit to a combination of basis spectra of protein, lipid, RNA, DNA, and glycogen as described in Sec. 2.7 to determine relative fractions of each component. Figures 3 and 4 show typical Raman spectra of live cells and dead cells at 24 hours, with their corresponding fit and fit residuals.

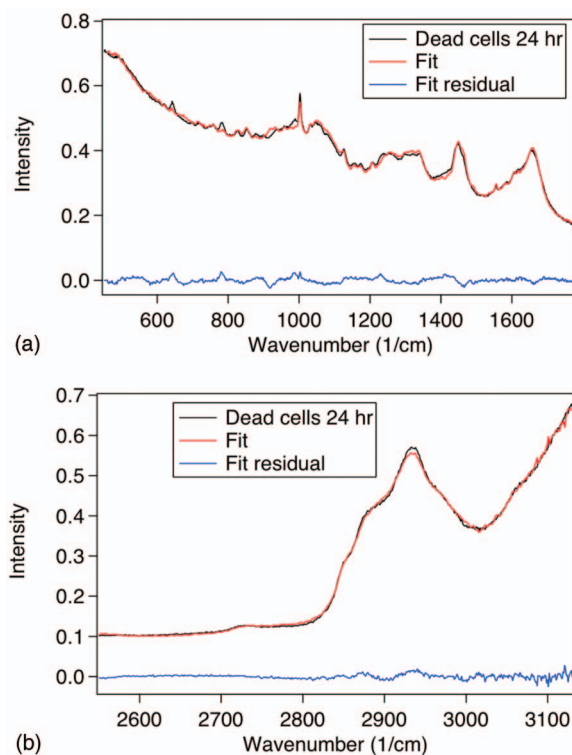


Fig. 4 Example of Raman data of dead cells (24-hour) and the corresponding fit and fit residual: (a) 450 to 1785 cm^{-1} , and (b) 2550 to 3130 cm^{-1} .

The relative fractions of each component were estimated from the fits and are shown in Fig. 5. The relative fractions of protein and DNA were higher, and the relative fraction of RNA and lipid lower for dead cells. Student's *t*-tests were performed to assess if the difference in the average values was significant. If the confidence level was less than 90%, the difference was considered nonsignificant (n.s.). Results of the *t*-tests are shown in Table 1.

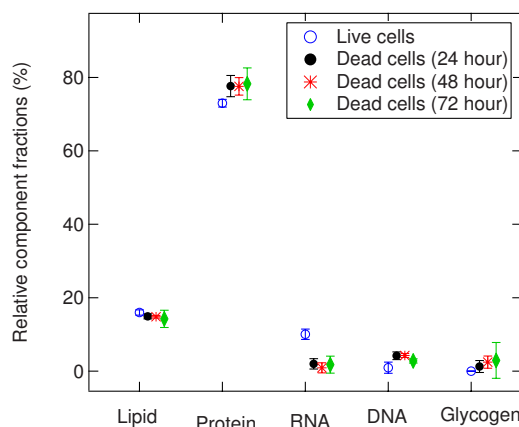


Fig. 5 Relative fractions of biochemical components in live and dead cells. Experiments on live cells, dead cells at 24 hours and dead cells at 48 hours were each repeated four times. Three duplicate experiments were performed for dead cells at 72 hours. The averages and standard deviations of the results of these experiments are shown.

Table 1 Student's t-test results for significance in the difference of the biochemical composition of dead cells compared to live cells.

	Dead: 24 hour	Dead: 48 hour	Dead: 74 hour
Lipid	>90%	>95%	n.s.
Protein	>95%	>95%	>90%
RNA	>99.9%	>99.9%	>99%
DNA	>95%	>99%	>90%
Glycogen	n.s.	>95%	n.s.

The residuals of the spectral fits (e.g., the residuals in Figs. 3 and 4) were not random noise. The average residuals of all of the fits were computed, and there were small systematic errors in the fits of both the live and dead cells. The systematic errors in fits to live cells have been noted and discussed previously.¹³ The average residuals of the fits to the 24-hour dead cell spectra were found to have some large peaks not present in the residuals of the live cells. Specifically, new positive peaks were found at 642, 781, 985, and 1230 cm^{-1} . Two of these peaks can be attributed to protein. The peak at 642 cm^{-1} has been attributed variously to the C-S stretch of methionine or cysteine¹⁹ and to tyrosine.^{20,21} Disordered protein has a peak at 1231 cm^{-1} .^{22,23} The peak at 781 cm^{-1} is the symmetric O-P-O diester stretch of DNA and RNA. The peak at 985 cm^{-1} is also likely due to RNA and DNA, since protein, lipid, and glycogen all have minuscule Raman intensities at 985 cm^{-1} .

3.4 Comparison of the Spectra of Live and Dead Cells

Raman spectra of live and dead cells were normalized to the peak value at 2933 cm^{-1} . The Raman intensity at 2933 cm^{-1} was due primarily to protein. Lipid and glycogen also had significant Raman intensities at 2933 cm^{-1} , while the nucleic acids had little Raman intensity at that wavenumber. Therefore, a difference in nucleic acid intensity in another region of the spectrum indicates a change in DNA or RNA content relative to the other constituents. Similarly, a difference in Raman intensity in another region of the spectrum where protein is the dominant Raman scatterer indicates a change in protein content relative to lipid and glycogen content. Analogous statements hold for lipid and glycogen.

The average and standard deviations of the Raman spectra of live cells and dead cells at 24 hours are shown in Fig. 6. The data shown are a compilation of four different experiments for each condition. Figure 6 demonstrates that there are some differences in the spectra of live and dead cells that are significantly greater than the variations seen in measuring either live or dead cells.

Figure 7 shows the average spectra of live cells and dead cells at 24, 48, and 72 hours. Spectra are shown without error bars for clarity. Spectra of dead cells at 48 and 72 hours showed similar changes to those at 24 hours, with some of the changes being more prominent in the dead cells at 72 hours.

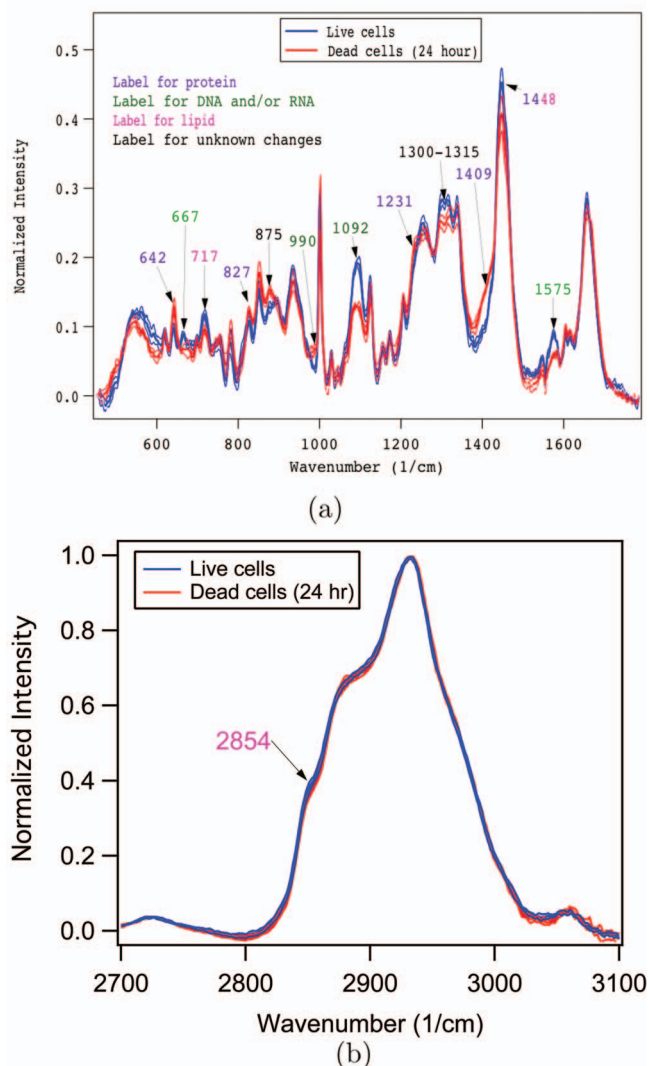


Fig. 6 Comparison of Raman spectra of live and dead cells (24-hour): (a) 450 to 1785 cm^{-1} , and (b) 2550 to 3130 cm^{-1} . The thick lines are average spectra. The thin lines are the plus and minus standard deviations.

Some of the differences between the live and dead cell spectra shown in Fig. 6 are consistent with the relative increase in protein concentration in the dead cells as determined by fitting the spectra to basis components (Fig. 5). There was a 31% increase at $\sim 642 \text{ cm}^{-1}$ in the average spectrum of cells dead for 24 hours. Dead cells (24-hour) also showed an increase of 13% in the peak intensity at 1231 cm^{-1} , which is primarily attributed to the disordered structure of protein.^{22,23} The 1395 to 1425 cm^{-1} region was more intense in dead cells compared to live cells. Raman intensity in this region is primarily due to protein, probably the deformation modes of CH_3 groups.²⁴ There is also a contribution from the ring-breathing modes of the adenine and guanine bases in DNA at 1421 cm^{-1} .^{19,23}

In addition to the change at 1421 cm^{-1} discussed above, which is consistent with the relative increase in DNA content, several of the differences in Fig. 6 are consistent with the overall decrease in nucleic acid content in the dead cells

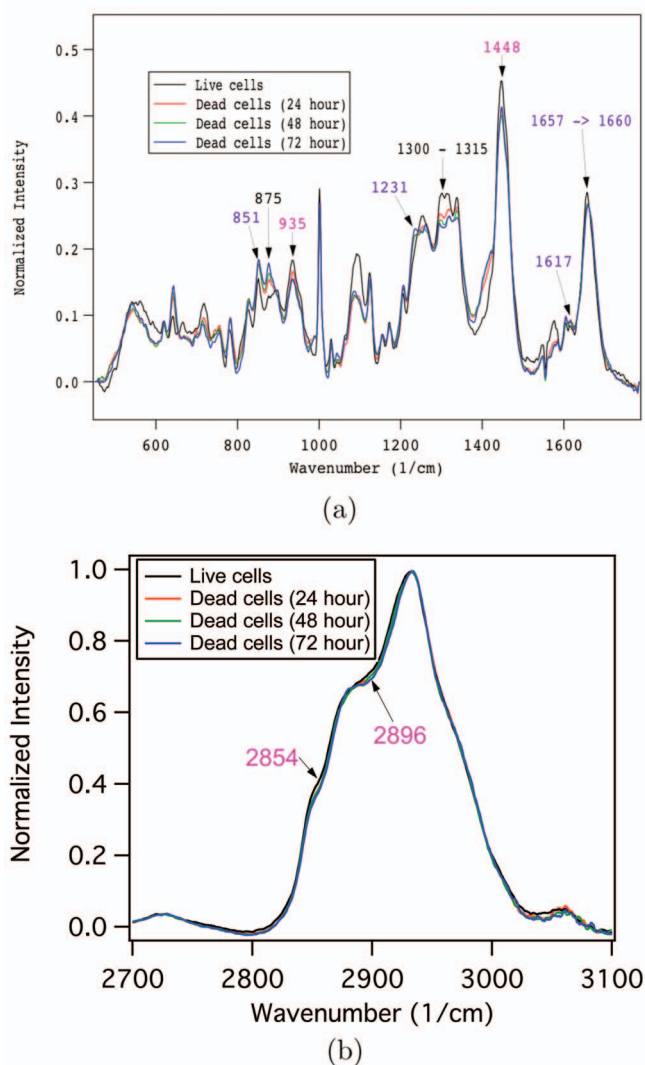


Fig. 7 Comparison of Raman spectra of dead cells at 24, 48, and 72 hours: (a) 450 to 1785 cm^{-1} , and (b) 2550 to 3130 cm^{-1} .

shown in Fig. 5. There was a 23% decrease in the region around 667 cm^{-1} in the average spectrum of cells dead for 24 hours. This peak had overlapping contributions from the guanine and thymine bases of DNA and RNA.¹⁹ There was a 35% decrease in Raman intensity in the region between 1558 and 1584 cm^{-1} for the dead cells. DNA and RNA both have dominant peaks in this region at $\sim 1575 \text{ cm}^{-1}$ that arise from the ring-stretching modes of adenine and guanine.^{19,23} A decrease at 990 cm^{-1} can be assigned to RNA. There was a decrease in the intensity from 1080 to 1100 cm^{-1} in the 24-hour dead cell spectrum. This region contains a $\sim 1092 \text{ cm}^{-1}$ peak arising from the symmetric PO_2^- stretching vibration of DNA and RNA,²³ a 1085 cm^{-1} peak arising from the PO_2^- stretching vibration of lipid,^{23,25,26} and C-C stretches of the hydrocarbon chain of phospholipids.^{23,27,28}

In addition to the changes in the 1085 to 1090 cm^{-1} region assigned to lipid, other changes were consistent with the relative decrease in lipid content shown in Fig. 5. A decrease of 19% was observed in the peak at $\sim 717 \text{ cm}^{-1}$ in the average spectrum of dead cells at 24 hours. This corresponds pri-

marily to the C-N stretch in the membrane phospholipid head end.^{23,29} A peak at 935 cm^{-1} decreased with time after OGD (Fig. 7), which we assigned to lipid. There appear to be decreases in intensity near 2854 cm^{-1} and 2896 cm^{-1} , both of which are lipid peaks. A peak at 1448 cm^{-1} also decreased after cell death. Both protein and lipid have strong Raman intensities at this wavelength, with lipid having the stronger intensity (on a per-weight basis). The decrease at this wavenumber is then consistent with a decrease in relative lipid concentration.

Several regions also showed significant changes that are difficult to interpret biochemically due to the overlap of Raman intensities of several biochemicals. The Raman intensity at 875 cm^{-1} increased with time after OGD (see Fig. 7). A peak at 877 cm^{-1} has been associated with the C-C stretching mode of lipid and hydroxyproline in protein.³⁰ The Raman spectrum of dead cells (24-hour) showed a decrease between 1300 and 1315 cm^{-1} . This region contains the CH_3/CH_2 twisting modes of lipid^{28,29} as well as significant Raman scattering from protein. DNA and RNA also have peaks in this region.

Analysis of the spectral changes can also provide insight into possible changes in the protein structure/composition. There is a shift in the amide I peak [Fig. 7(a)] from $\sim 1657 \text{ cm}^{-1}$ in live cells to $\sim 1660 \text{ cm}^{-1}$ in dead cells at 72 hours. This shift may indicate an increase in disordered structure. An amide I vibration at 1665 cm^{-1} has been assigned to disordered structure.³¹ An increase was noted in a protein band associated with a disordered structure of protein ($\sim 1231 \text{ cm}^{-1}$) with cell death [Fig. 7(a)]. In addition to the significant changes at 642 cm^{-1} and $\sim 827 \text{ cm}^{-1}$ (Fig. 6), a small increase (not outside the error bars) in the dead cell spectra at 851 cm^{-1} and $\sim 1617 \text{ cm}^{-1}$ (Fig. 7) can be at least partially assigned to tyrosine. However, no differences were found in the intensity of the phenylalanine peak at $\sim 1001 \text{ cm}^{-1}$. This indicates a change in the spectra of protein.

4 Discussion and Conclusions

The mechanism used to cause cell death used in this work, oxygen and glucose deprivation, is believed to cause necrosis rather than apoptosis.^{12,32} Apoptosis (or programmed cell death) is dependent on caspase activation. Caspase activation is an energy-dependent process, and in the absence of energy, apoptosis cannot proceed. Nicotera et al. demonstrated that the level of ATP acts as a switch between apoptosis and necrosis.³³ OGD has been shown to induce necrosis in 3-D "sandwich" models of 9L and V70 cells.¹² The authors concluded that "A joint oxygen-glucose deprivation model for necrosis seems reasonable: cells which are short of oxygen alone can use anaerobic glycolysis; cells which are short of glucose alone can catabolize other substances provided they can carry out sufficient oxidative phosphorylation; but there is no obvious energy-generating mechanism for cells which are short of both." Extensive previous work with multicellular spheroids has also shown that central necrosis in this 3-D tumor model results from combined deprivation of oxygen and glucose.³² Results from this model also demonstrate that necrosis in tumors primarily occurs in nonproliferating cells.³⁴ We have previously demonstrated differences in the Raman

spectra of proliferating and quiescent cells,^{14,15} so the use of nonproliferating cells in these experiments not only corresponds more closely with the situation in tumors, but also avoids complications from a changing proliferative status during oxygen and glucose deprivation.

In tissue, several types of necrosis can occur, with the most common forms being coagulative necrosis and liquefactive necrosis. Coagulative necrosis occurs when the catalytic enzymes that destroy the cell are derived from the lysosomes of the dead cells (autolysis). Liquefactive necrosis occurs when the catalytic enzymes come from immigrant leukocytes (heterolysis). For the cell model used in this work, coagulative necrosis occurred since no leukocytes were present. In coagulative necrosis, the outline of the cells persists at least for some days, although there is clear damage to the plasma membrane, to cytoplasmic organelles, and to structural matrix proteins early on. In the process of coagulative necrosis, nuclear changes occur including pyknosis (shrinkage of the nucleus), karyorrhexis (fragmentation of chromatin), and karyolysis (DNase activity destroying DNA). It generally takes a day or two for the nucleus to totally disappear. Evidence for coagulative necrosis as the mechanism of cell death in tumors comes from studies in multicellular spheroids: examination of histological sections of spheroids reveals a layer of pyknotic nuclei in the necrotic center immediately adjacent to the viable cells.³² Regions of necrosis that are farther from the viable cell rim do not contain identifiable nuclei, presumably due to their degradation with time. The presence of pyknotic nuclei in regions of human tumor necrosis has been known for some time (e.g., Ref. 35).

Our results (Fig. 5) indicate that in the first few days of necrosis, lipid and RNA are degraded and the Raman intensities from these compounds decrease relative to the Raman intensities from protein and DNA. These results are consistent with the known process of coagulative necrosis, in which destruction of cytoplasmic structures and degradation of the membranes occurs first. At 72 hours, the Raman results (Fig. 5) indicate that DNA is being destroyed consistent with the known process of destruction of nuclei in necrosis. Evidence also exists for changes in the conformation and composition of the biochemical components. The residuals of the spectral fits contain peaks that can be attributed to specific components of nucleic acids and protein. There is a shift of the amide I peak between the live and dead cells, and the Raman intensities of bands of tyrosine and phenylalanine do not show the same trends, both indicating changes in protein conformation or composition.

4.1 Comparison to Previous Work

The results we obtained differ somewhat from previous studies of cell death by vibrational spectroscopy. Jamin et al. reported that the IR bands of a necrotic cell were broader than those observed for viable cells, and they noted the appearance of a new, narrow band at 1730 cm⁻¹.³⁶ In a subsequent study, Jamin and coworkers did not see any new peaks in the vicinity of 1730 cm⁻¹.³⁷ The spectra of the necrotic cells were significantly varied, although some common features were observed: increases at 1222 and 1044 cm⁻¹.³⁷ The IR 1222 cm⁻¹ peak is an asymmetric PO₂⁻ stretching band present in RNA, DNA, and lipid. An increase at 1222 cm⁻¹

appears contradictory to our results in that two of the primary contributors to this band.—RNA and lipid—decreased relative to protein concentration. The assignment of the 1044 cm⁻¹ IR band is unknown. A strong band at that wavenumber is not present in RNA, DNA, lipid, or protein, although there is a symmetric PO₂⁻ stretching band at 1054 cm⁻¹ in RNA. Potentially, differences in results could be attributed to differences in how the necrosis was induced or in the time between necrosis induction and spectroscopy measurements. In the two Jamin studies, necrosis was induced by allowing cell cultures to grow until a large percentage of cells had died; thus, the cells were deprived of nutrients. Necrotic cells failed the trypan blue exclusion test.

Notingher et al. made Raman microspectrometry measurements of live and dead human lung epithelial cells.²⁸ Dead cells were extracted from fresh medium by visual inspection and failed the trypan blue exclusion test. They found that the spectrum of dead cells showed decreases in the peaks of nucleic acids corresponding to the breakdown of phosphodiester bond and DNA bases, specifically at 782 cm⁻¹, 788 cm⁻¹, and 1095 cm⁻¹. (The spectra were normalized to the 1449 cm⁻¹ peak, which is dominated by protein and lipid. Lipid shows a slightly stronger intensity at 1449 cm⁻¹ than protein.) They observed a 45% decrease in the intensity of the phenylalanine peak, in contrast to the results presented here for MEL-28 cells, which showed no change in the phenylalanine peak. Alterations corresponding to protein conformational changes were also observed. The peak at 1231 cm⁻¹ attributed to random coils was found to decrease by 66%. In contrast, in this study necrotic MEL-28 cells had an increased intensity 1231 cm⁻¹ relative to live MEL-28 cells. Differences in the wavenumber region 1190 to 1385 cm⁻¹ indicated a decrease in the amount of nucleic acids and proteins. The decrease in nucleic acid content is consistent with the results presented here, but an increase rather than a decrease in protein content was observed. A 10 cm⁻¹ decrease in the half-maximum width of the amide I band was also observed. In contrast, for our MEL-28 cells, the amide I band was found to shift by 3 cm⁻¹ toward the higher wavenumbers in spectra of dead cells with no decrease in width.

Gasparri and Muzio used attenuated total reflection Fourier transform infrared (ATR-FTIR) spectroscopy to measure biochemical changes occurring due to necrosis in HL60 leukemia cells.³⁸ Necrosis was induced by heat shock or oxidative stress by the addition of hydrogen peroxide. The cells were measured as a dehydrated biofilm. Dehydration has been shown to alter IR spectra³⁹ and may obscure some changes due to necrosis. They observed an increase in the area ratio of amide I/amide II and a decrease in the overall intensity of the region assigned to nucleic acids (relative to amide I). A shoulder on amide I centered at 1621 cm⁻¹ was present in the necrotic cells but not in the viable cells. The decrease in intensity of regions associated with nucleic acids is consistent with our results. The changes in amide I and the change in amide I/amide II indicate a change in average protein structure. Our results also indicate some change in average protein structure.

Some work has been done on the spectroscopic identification of tumor necrosis in tissue samples. Raman spectroscopy has been used to discriminate vital tumor from necrotic tissue in tissue samples of human glioblastoma.⁴⁰ Biochemical dif-

ferences between necrosis and vital tissue were obtained by the analysis of the difference Raman spectra. It was found that necrotic tissue consistently had higher levels of cholesterol, cholesterol esters, and carotenoids. Shafer-Peltier et al. made Raman spectroscopy measurements on breast cancer necrosis of three patients.⁴¹ The composition of necrosis was found to vary from location to location even within a single duct. Necrotic regions were found to contain fat, collagen, calcification (calcium hydroxyapatite), free cholesterol, and cholesterol ester (linoleate) along with cellular debris. Breast tissue is complex and contains several different cell types. The variation in the composition of necrosis at various locations was attributed to the heterogeneous composition of breast tissue. The common theme for necrotic tissue appears to be an increase in lipid/cholesterol/fat content, which was not seen in this study of cells. Potentially, this difference is due to the presence of leukocytes in tissue. Additionally, the necrotic tissue was measured at a longer time after cell death than in our cell studies.

4.2 Conclusions

Raman spectroscopy of live, plateau-phase MEL-28 cells and necrotic MEL-28 cells demonstrated that there are relative decreases in lipid and RNA content with a corresponding relative increase in protein content in the first days after necrosis induced by oxygen and glucose deprivation. The spectral results also indicate that there are conformational protein changes, changes in nucleic acid conformation, and that the degradation of DNA may begin between 48 and 72 hours. The analyses leading to these results were fits of the spectra to basis spectra of RNA, DNA, lipid, protein, and glycogen, and a visual examination of the spectra to look for changes in peak intensities and positions. The basis spectra analysis has the advantage that correlations in changes at different wavenumbers corresponding to the same biochemical component are intrinsically accounted for and used. The disadvantage of using basis spectra is that changes in conformation of biochemical components that affect spectral shapes of the component spectra (e.g., peak positions) are not accounted for. By examining the fit residuals and visual examination of the spectra, evidence for changes in the biochemicals themselves was obtained.

The results of several reports in the literature of vibration spectroscopy measurements of live and necrotic cells vary greatly. Possible reasons for the variation include experimental error (e.g., hydration state; subtraction of background, which is fluorescence for Raman and water for IR); the method by which necrosis was induced; whether lysed and whole cells or just whole cells were measured; the amount of time the cells were dead; and the cells' environment after death. The environment is very different for tissue measurements as opposed to cell measurements. In the tissue environment, an increase in lipid is a common theme in the literature.

The differences in the Raman spectra of live and dead cells can be used to monitor the health and viability of cells in large-scale cell and tissue culture. Another potential application is monitoring the effect of antitumor drugs on quiescent cells. An improved understanding of how environment affects the biochemical changes during and after cell death would facilitate these applications.

Acknowledgments

This work was supported by NIH-NCI Grant No. CA89255. The flow cytometry experiments were made possible by the National Flow Cytometry Resource at Los Alamos New Mexico (NIH-NCRR Grant No. RR01315).

References

1. W. S. Ahn, S. M. Bae, S. W. Huh, J. M. Lee, S. E. Namkoong, S.-J. Han, C. K. Kim, J.-K. Kim, and Y.-W. Kim, "Necrosis-like death with plasma membrane damage against cervical cancer cells by photodynamic therapy," *Int. J. Gynecol. Canc.* **14**(3), 475–482 (2004).
2. E. R. Fischer et al., "Pathologic findings from the National Surgical Adjuvant Breast Project protocol B-06: 10-year pathologic and clinical prognostic discriminants," *Cancer* **71**(8), 2507–2514 (1993).
3. R. T. Pu, A. F. Schott, D. E. Sturtz, K. A. Griffith, and C. G. Kleer, "Pathologic features of breast cancer associated with complete response to neoadjuvant chemotherapy—Importance of tumor necrosis," *Am. J. Surg. Pathol.* **29**(3), 354–358 (2005).
4. N. J. Lindner, M. T. Scarborough, S. S. Spanier, and W. F. Enneking, "Local host response in osteosarcoma after chemotherapy referred to radiographs, computer tomography, tumour necrosis and patient survival," *J. Cancer Res. Clin. Oncol.* **124**(10), 575–580 (1998).
5. P. Picci, B. T. Rougraff, G. Bacci, J. R. Neff, L. Sangiorgi, A. Cazzola, N. Baldini, S. Ferrari, and M. Mercuri, "Prognostic significance of histopathologic response to chemotherapy in nonmetastatic Ewing's sarcoma of the extremities," *J. Clin. Oncol.* **11**(9), 1763–1769 (1993).
6. G. Rosen, B. Caparros, A. G. Huvos, C. Kosloff, A. Nirenberg, A. Cacavio, R. C. Marcove, J. M. Lane, B. Mehta, and C. Urban, "Preoperative chemotherapy for osteogenic-sarcoma—Selection of postoperative adjuvant chemotherapy based on the response of the primary tumor to preoperative chemotherapy," *Cancer* **49**(6), 1221–1230 (1982).
7. V. F. H. Chong, Y. F. Fan, and J. B. K. Khoo, "MRI features of cervical nodal necrosis in metastatic disease," *Biomedicine* **12**(3), 123–138 (1999).
8. S. J. Nelson, D. B. Vigneron, and W. P. Dillon, "Serial evaluation of patients with brain tumors using volume MRI and 3 D 1 H MRSI," *Clin. Radiol.* **51**(2), 103–109 (1996).
9. M. Principi, M. Italiani, A. Guiducci, I. Aprile, M. Muti, G. Giulianelli, and P. Ottaviano, "Perfusion MRI in the evaluation of the relationship between tumour growth, necrosis and angiogenesis in glioblastomas and grade 1 meningiomas," *Neuroradiology* **45**(4), 205–211 (2003).
10. A. J. Kumar, N. E. Leeds, G. N. Fuller, P. Van Tassel, M. H. Maor, R. E. Sawaya, and V. A. Levin, "Malignant gliomas: MR imaging spectrum of radiation therapy and chemotherapy induced necrosis of the brain after treatment," *Radiology* **217**(2), 377–384 (2000).
11. J. P. Rock, D. Hearshen, L. Scarpace, D. Croteau, J. Gutierrez, J. L. Fisher, M. L. Rosenblum, and T. Mikkelsen, "Correlations between magnetic resonance spectroscopy and image-guided histopathology, with special attention to radiation necrosis," *Neurosurgery* **51**(4), 912–920 (2002).
12. L. Hlatky, R. K. Sachs, and E. L. Alpen, "Joint oxygen-glucose deprivation as the cause of necrosis in a tumor analog," *J. Cell Physiol.* **134**(2), 167–178 (1988).
13. J. R. Mourant, K. W. Short, S. Carpenter, N. Kunapareddy, L. Coburn, T. M. Powers, and J. P. Freyer, "Biochemical differences in tumorigenic and nontumorigenic cells measured by Raman and infrared spectroscopy," *J. Biomed. Opt.* **10**(3), 31106–31115 (2005).
14. K. W. Short, S. Carpenter, J. P. Freyer, and J. R. Mourant, "Raman spectroscopy detects biochemical changes due to proliferation in mammalian cell cultures," *Biophys. J.* **88**(6), 4274–4288 (2005).
15. J. R. Mourant, J. Dominguez, S. Carpenter, K. W. Short, T. M. Powers, R. Michalczyk, N. Kunapareddy, A. Guerra, and J. P. Freyer, "Comparison of vibrational spectroscopy to biochemical and flow cytometry methods for analysis of the basic biochemical composition of mammalian cells," *J. Biomed. Opt.* **11**(6), 64024–64035 (2006).
16. J. R. Mourant, A. H. Hielscher, A. A. Eick, T. M. Johnsont, and J. P. Freyer, "Evidence of intrinsic differences in the light scattering properties of tumorigenic and nontumorigenic cells," *Cancer Genet. Cytogenet.* **84**(6), 366–374 (1998).
17. P. R. Bevington and D. K. Robinson, *Data Reduction and Error*

- Analysis for the Physical Sciences*, McGraw-Hill, Boston (1992).
18. J. P. Freyer and R. M. Sutherland, "A reduction in the *in situ* rates of oxygen and glucose consumption of cells in EMT6/RO spheroids during growth," *J. Cell Physiol.* **124**(3), 516–524 (1985).
 19. J. W. Chan, D. S. Taylor, T. Zwerdling, S. M. Lane, K. Ihara, and T. Huser, "Micro-Raman spectroscopy detects individual neoplastic and normal hematopoietic cells," *Biophys. J.* **90**(2), 648–656 (2006).
 20. C. Medina-Gutiérrez, C. Frausto-Reyes, J. L. Quintanar-Stephano, and R. Sato-Berrú, "Amino acid contents along the visual and equatorial axes of a pig lens by Raman spectroscopy," *Spectrochim. Acta, Part A* **60**(10), 2269–2275 (2004).
 21. M. Tsuboi, K. Ushizawa, K. Nakamura, J. M. Benevides, S. A. Overman, and G. J. Thomas, Jr., "Orientations of Tyr 21 and Tyr 24 in the capsid of filamentous virus Ff determined by polarized Raman spectroscopy," *Biochemistry* **40**(5), 1238–1247 (2001).
 22. T. G. Spiro and B. P. Gaber, "Laser Raman scattering as a probe of protein structure," *Annu. Rev. Biochem.* **197**(46), 553–572 (1977).
 23. F. S. Parker, *Applications of Infrared, Raman, and Resonance Raman Spectroscopy in Biochemistry*, Springer, (1983).
 24. B. W. Barry, H. G. M. Edwards, and A. C. Williams, "Fourier transform Raman and infrared vibrational study of human skin: assignment of spectral bands," *J. Raman Spectrosc.* **23**, 641–645 (1992).
 25. L. K. Tamm and S. A. Tatulian, "Infrared spectroscopy of proteins and peptides in lipid bilayers," *Q. Rev. Biophys.* **30**(04), 365–429 (1997).
 26. J. Florian, V. Baumruk, M. Strajbl, L. Bednarova, and J. Stepanek, "IR and Raman spectra, conformational flexibility, and scaled quantum mechanical force fields of sodium dimethyl phosphate and dimethyl phosphate anion," *J. Phys. Chem.* **100**(5), 1559–1568 (1996).
 27. S. Fendel and B. Schrader, "Investigation of skin and skin lesions by NIR-FT-Raman spectroscopy," *Fresenius' J. Anal. Chem.* **360**(5), 609–613 (1998).
 28. I. Notingher, S. Verrier, S. Haque, J. M. Polak, and L. L. Hench, "Spectroscopic study of human lung epithelial cells (A549) in culture: Living cells versus dead cells," *Biospectroscopy* **72**, 230–240 (2003).
 29. N. Stone, C. Kendall, N. Shepherd, P. Crow, and H. Barr, "Near-infrared Raman spectroscopy for the classification of epithelial precancers and cancers," *J. Raman Spectrosc.* **33**(7), 564–573 (2002).
 30. Z. Huang, A. McWilliams, H. Lui, D. I. McLean, S. Lam, and H. Zeng, "Near-infrared Raman spectroscopy for optical diagnosis of lung cancer," *Int. J. Cancer* **107**(6), 1047–1052 (2003).
 31. W. L. Peticolas, "Raman spectroscopy of DNA and proteins," *Methods Enzymol.* **246**, 389–416 (1995).
 32. J. P. Freyer, "Regulation of growth saturation and development of necrosis in EMT6/RO multicellular spheroids by the glucose and oxygen supply," *Cancer Res.* **46**(7), 3504–3512 (1986).
 33. P. Nicotera, M. Leist, and E. Ferrando-May, "Intracellular ATP, a switch in the decision between apoptosis and necrosis," *Toxicol. Lett.* **102**(103), 139–142 (1998).
 34. J. P. Freyer and R. M. Sutherland, "Proliferative and clonogenic heterogeneity of cells from EMT6/RO multicellular spheroids induced by the glucose and oxygen-supply," *Cancer Res.* **46**(7), 3513–3520 (1986).
 35. G. C. Stowe, Z. N. Zakov, D. M. Albert, T. R. Smith, D. N. Sang, and J. L. Craft, "Vascular basophilia in ocular and orbital tumors," *Invest. Ophthalmol. Visual Sci.* **18**(10), 1068–1075 (1979).
 36. N. Jamin, P. Dumas, J. Moncuit, W. H. Fridman, J. L. Teillaud, G. L. Carr, and G. P. Williams, "Highly resolved chemical imaging of living cells by using synchrotron infrared microspectrometry," *Proc. Natl. Acad. Sci. U.S.A.* **95**(9), 4837–4840 (1998).
 37. N. Jamin, L. Miller, J. Moncuit, W. H. Fridman, P. Dumas, and J. L. Teillaud, "Chemical heterogeneity in cell death: Combined synchrotron IR and fluorescence microscopy studies of single apoptotic and necrotic cells," *Biospectroscopy* **72**(5), 366–373 (2003).
 38. F. Gasparri and M. Muzio, "Monitoring of apoptosis of HL60 cells by Fourier-transform infrared spectroscopy," *Biochem. J.* **369**(2), 239–248 (2003).
 39. J. R. Mourant, R. R. Gibson, T. M. Johnson, S. Carpenter, K. W. Short, Y. R. Yamada, and J. P. Freyer, "Methods for measuring the infrared spectra of biological cells," *Phys. Med. Biol.* **48**(2), 243–257 (2003).
 40. S. Koljenovic, L. P. Choo-Smith, T. C. B. Schut, J. M. Kros, H. J. Van den Berge, and G. J. Puppels, "Discriminating vital tumor from necrotic tissue in human glioblastoma tissue samples by Raman spectroscopy," *Lab. Invest.* **82**(10), 1265–1277 (2002).
 41. K. E. Shafer-Peltier, A. S. Haka, M. Fitzmaurice, J. Crowe, J. Myles, R. R. Dasari, and M. S. Feld, "Raman microspectroscopic model of human breast tissue: implications for breast cancer diagnosis *in vivo*," *J. Raman Spectrosc.* **33**(7), 552–63 (2002).